

Venturing into Unexplored Phase Space: Synthesis, Structure, and Properties of MgCo_3B_2 Featuring a Rumped Kagomé Network

Paul Oftedahl, Nawsher J. Parvez, Zhen Zhang, Yang Sun, Vladimir Antropov, John Q. Xiao, and Julia V. Zaikina*



Cite This: *Chem. Mater.* 2024, 36, 9834–9847



Read Online

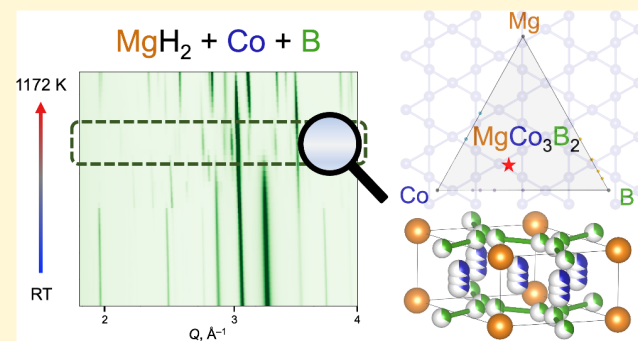
ACCESS |

Metrics & More

Article Recommendations

Supporting Information

ABSTRACT: MgCo_3B_2 , a novel ternary boride in a previously unexplored phase space, was synthesized using the hydride route. In situ powder X-ray diffraction and DFT calculations aided in the discovery of this compound, whose structure was then determined by single-crystal X-ray diffraction. Like the closely related CeCo_3B_2 , MgCo_3B_2 crystallizes in centrosymmetric space group $P6/mmm$ ($a = 4.883(2)$ Å, $c = 2.926(2)$ Å at 210 K, $Z = 1$). Unlike CeCo_3B_2 , however, it adopts a disordered structure that features a rumped Kagomé network of Co atoms, and Mg atoms fill the channels of a Co–B framework. Although the structural disorder leads to motifs that are similar to those observed in MgNi_3B_2 and other related ternary borides, no evidence of an ordered superstructure was found by single-crystal X-ray diffraction or high-resolution powder X-ray diffraction. In the case of CeCo_3B_2 , boron atoms occupy the center of regular Co_6 trigonal prisms; in MgCo_3B_2 , boron atoms are shifted from the center of the prism to form B–B dimers with roughly the same length as those found in MgNi_3B_2 . Magnetic susceptibility data exhibit an unusual temperature dependence that cannot be convincingly modeled by the modified Curie–Weiss equation, consistent with DFT calculations predicting a nonmagnetic ground state. Intrinsic susceptibility at 300 K is 1.42×10^{-3} emu/mol Oe, which is comparable to that of paramagnetic YCo_3B_2 and CeCo_3B_2 with a similar structure and composition. This study showcases the efficacy of combining several methodologies to discover new solids in unexplored phase spaces. This approach includes in situ PXRD data to monitor reactions of precursors upon heating, a diffusion-enhanced synthesis method, and DFT assessment of compound stability.



INTRODUCTION

Borides are a class of materials whose diversity of structural motifs and compositional possibilities undergird a range of chemical and physical properties that make them relevant to a wide variety of technological applications.^{1–3} Intermetallic borides and boron–metal alloys have long received attention for their outstanding physical properties such as ultrahardness and mechanical and thermal stability. Notable electrocatalytic and magnetic properties have been reported for binary and ternary intermetallic borides, including MoB_2 as a catalyst for the hydrogen evolution reaction,⁴ $\text{Nd}_2\text{Fe}_{14}\text{B}$ displaying high magnetic coercivity,⁵ and AlFe_2B_2 exhibiting substantial magnetocaloric effect.^{6,7} Boron-rich borides have been reported to exhibit superconductivity (MgB_2 ,⁸ YB_6)⁹ and have the potential to exhibit significant thermoelectric effect owing to their complex crystal and electronic structures.^{2,10}

Synthesis of borides is complicated by a number of factors: high temperatures are typically used owing to the inertness and high melting point of boron, but doing so tends to bypass metastable phases and can induce reactions with the container material.^{2,11} This problem is compounded in the case of

ternary borides containing an alkali or alkaline-earth metal (A) and a transition metal, where the differences in ductility, reactivity, and melting point between the A metals and boron work against the formation of the desired phases.^{12,13} Of the systems A -T-B, compounds with $T = \text{Ni}$ are known for $A = \text{Li}$, Mg , Ca , Sr , and Ba , with $\text{Mg}_3\text{Ni}_{20}\text{B}_6$ being the first example reported in 1963.¹⁴ However, no ternary A -T-B borides with a first-row transition metal other than nickel have been published to date. Arc-melting elemental precursors in an inert atmosphere, a common approach to the synthesis of intermetallic borides in crystalline form, is not possible in these cases due to the high volatility of the A metal.^{1,13}

Our key to expanding the compositional diversity of A -T-B compounds is the hydride route, where an alkali or alkaline-

Received: July 17, 2024

Revised: September 16, 2024

Accepted: September 17, 2024

Published: September 27, 2024



earth metal hydride is used in place of the metal itself. Substitution of a brittle, salt-like alkali or alkaline-earth metal hydride AH or AH₂ for a ductile metal permits precise compositional control and facilitates intimate mixing of precursors. This helps alleviate the kinetic hindrances inherent to solid-state reactions and enables rapid screening of new ternary systems by allowing reactions to proceed in less time and at lower temperatures.^{15,16} The hydride route also facilitates the use of *in situ* monitoring of reactions via synchrotron powder X-ray diffraction, a technique that helps pinpoint the optimal synthesis temperature to produce a desired phase.¹⁷ The search for new borides is further aided by DFT calculations of formation energy, electronic structure, and relevant properties such as magnetic ordering. Ultimately, *in situ* reaction monitoring and computational assessment of structure stability help eliminate the trial-and-error approach to the search for new solids.¹⁸

Recently, our group has confirmed computational predictions of new compounds in the Li–Ni–B system, and substitution studies have expanded to the quaternary Li–Ni–Co–B system.^{12,19–21} However, despite theoretical predictions of stability and metastability, phases in the Li–Co–B ternary system have remained elusive.²² Therefore, we decided to expand our efforts into the Mg–Co–B phase space, where no ternary compounds have hitherto been reported. An exploratory *in situ* powder X-ray diffraction experiment hinted at the formation of a ternary compound with a structure resembling MgNi₃B₂.^{23,24} These findings were reinforced by DFT calculations indicating a low formation energy for the cobalt analog of MgNi₃B₂, which was further confirmed by *ex-situ* laboratory synthesis.

With respect to the potential properties of new ternary phases, switching from Ni to Co is advantageous due to the lower filling of the 3d band, increasing the likelihood of exchange interactions leading to long- or short-range magnetic order. Furthermore, the structure of MgNi₃B₂ has a variety of features that prompt further exploration of the substitution of Ni for another first-row transition metal. MgNi₃B₂ is a chiral intermetallic that crystallizes in space group P6₄22; moreover, it features a slightly distorted, nonflat Kagomé network of Ni atoms, owing to the lack of mirror symmetry. The geometry of the Kagomé network, which consists of a 2D net of corner-sharing equilateral triangles, precludes the formation of an antiferromagnetic ground state with alternating up and down spins within a single layer, since not all pairs of spins can align in an antiparallel fashion. This could lead to magnetic frustration and related phenomena such as spin-glass or spin-ice states, superconductivity, charge-density waves, or potentially a quantum spin liquid state.^{25,26} On the other hand, the distinctive symmetry of the network has implications for electronic structure, giving rise to phenomena such as massive and massless Dirac Fermions and flat bands.^{27–29}

■ EXPERIMENTAL SECTION

Synthesis of Polycrystalline MgCo₃B₂ Powder. MgCo₃B₂ can be synthesized using both magnesium hydride and elemental magnesium Mg as the magnesium source. All precursors were manipulated in an argon-filled glovebox with an oxygen level below 1 ppm. For hydride synthesis, the following precursors were used: magnesium hydride (MgH₂, Sigma-Aldrich, hydrogen storage grade), cobalt powder (Co, Alfa Aesar, 1.6 μm, 99.8% trace metals basis), boron powder (B, Sigma-Aldrich, crystalline, 60 mesh, 99% trace metals basis) in the experimentally optimized ratio MgH₂:Co:B = 1.9:3:2.4 and total loading of 0.3 g. The powders were placed in

polystyrene grinding vials with slip-on caps and sealed inside two polypropylene bags in an argon atmosphere, then brought out of the glovebox. A SPEX Sample Prep 8000 M MIXER/MILL was used to ball-mill the powders for 18 min, after which the precursor mixture was placed in a niobium tube (roughly 1 cm diameter, 5 cm length) and sealed by arc-welding the end shut in an argon atmosphere.

For elemental synthesis, magnesium turnings (Mg, Alfa Aesar, 99.98%) washed with aqueous HCl were used in place of magnesium hydride along with the same cobalt and boron precursors in the experimentally optimized ratio Mg:Co:B = 2:3:2.4. Since Mg turnings cannot be easily ball-milled, only the Co and B powders were ball-milled (as described above). The Co/B precursor mixture was weighed before being placed in the bottom of a niobium tube, on top of which the magnesium turnings were placed. After weighing the Co/B mixture, the amount of magnesium was calculated to ensure a 2:3 ratio of magnesium to cobalt with a total typical mass of 0.3 g. At this point, the niobium tube was sealed under argon by arc-welding the end shut and was kept as vertical as possible until loading in the reactor.

For both synthesis routes, the sealed niobium tube was loaded into a silica reactor equipped with a Swagelok check valve to prevent the buildup of positive pressure in case of the release of hydrogen gas from the hydride reaction. The reactor was evacuated below 3.5×10^{-5} bar and placed into a resistance furnace (Thermo Scientific Thermolyne Type FD1500M) connected to a thermocontroller (Eurotherm 3216) and heated at 1.5 K/min to 1023 K, kept at that temperature for 48 h, and cooled by switching off the furnace. The byproduct of hydrogen gas embrittles the inside of the niobium tube but without compromising its structural integrity. To remove unreacted magnesium, the resulting powders were washed in dilute hydrochloric acid (pH between 1 and 2), rinsed with water and ethanol, and dried under vacuum.

Synthesis of MgCo₃B₂ Single Crystal. In an attempt to obtain crystals of a suitable size for laboratory single-crystal X-ray diffraction (SC-XRD), the same synthesis procedure as described above for a precursor of elemental magnesium was used, with the following modifications: (1) an additional excess of magnesium was used, with the resulting ratio Mg:Co:B = 2.5:3:2.4, and (2) the following temperature profile was used: heating at 1.25 K/min to 1173 K, holding at that temperature for 48 h, cooling at 0.1 K/min to 1073 K, holding at that temperature for 100 h, cooling at 0.13 K/min to 673 K, and turning off the furnace. Due to the excess of magnesium, the resulting mass was firmly adhered to the bottom of the Nb tube, so the tube was opened at both ends and placed in mild HCl (pH ≈ 1) until the mass had broken free of the tube. A crystal suitable for SC-XRD was selected after rinsing samples with water and ethanol, drying in air, and gently crushing to break up large agglomerates.

Laboratory Powder X-ray Diffraction. Routine phase analysis of powdered samples was performed on powder diffractograms acquired using a Rigaku MiniFlex600 powder diffractometer with Cu K_α radiation ($\lambda = 1.54051 \text{ \AA}$) and a Ni K_β filter. Zero-background plate holders composed of silica or a silicon single crystal were used to collect data at room temperature, and detector settings were chosen to minimize fluorescence of cobalt.

High-Resolution Powder X-ray Diffraction. High-resolution powder X-ray diffraction (HR-PXRD) measurements were acquired at the Low-Energy Wiggler beamline (WLE) of the Brockhouse Diffraction Sector at the Canadian Light Source at wavelength $\lambda = 0.81931 \text{ \AA}$ at room temperature. A sample of MgCo₃B₂ prepared from elemental magnesium was loaded in a silica capillary (0.5 mm inner diameter, 0.7 mm outer diameter) and sealed under vacuum. The capillary was mounted horizontally on a magnetic stub and spun during measurement at a rate of 2 Hz. Rietveld refinement of the powder diffractogram was carried out using the software GSAS-II.³⁰

Single-Crystal X-ray Diffraction. A suitable crystal was isolated from a sample prepared as described above, from which diffraction data were collected up to $2\theta = 90^\circ$ for a theoretical resolution of 0.50 Å. This was done in an effort to obtain high-angle reflections to aid in determining the absolute structure in case the crystal turned out to adopt a chiral structure, as is the case for MgNi₃B₂.²⁴ Data were

Table 1. Structural Parameters of MgCo₃B₂ as Refined from Single-Crystal XRD Data at 210 K^a

temperature		<i>a</i> (Å)	<i>c</i> (Å)	<i>V</i> (Å ³)
210 K		4.883(2)	2.926(2)	60.42(6)
298 K		4.89245(2)	2.93110(1)	60.7594(3)
atom	Wyckoff site	<i>x/a</i>	<i>y/b</i>	<i>z/c</i>
Co1	3g	0.5	0	0.5
Co2	6i	0.5	0	0.382(1)
Mg1	1a	0	0	0
B1	6l	0.6106(6)	0.221(1)	0
				s.o.f. <i>U</i> _{eq}
				0.0065(4) 0.0065(4) 0.0095(3) 0.0061(7) ^b

^aUnit cell parameters from SCXRD and from high-resolution powder XRD at 298 K are compared. Anisotropic ADPs for Co and Mg atoms are given in Table S3. ^b*U*_{iso} is used.

collected at 210 K on a Bruker D8 Venture diffractometer equipped with a Photon CMOS detector and cooled by an Oxford Cryosystem 800 low-temperature device, with a Mo Kα $\lambda/2$ radiation microsource giving a wavelength of 0.71073 Å.

Indexing by means of difference vectors in APEX3 software suggested a small hexagonal cell with $a = b = 4.88$ Å, $c = 2.93$ Å, equivalent to that adopted by CeCo₃B₂ and other RC₃B₂ compounds. After integrating and scaling SCXRD data in this small hexagonal cell to correct for absorption effects with SADABS,³¹ XPREP software calculated a value of $|E^2 - 1| = 0.964$, remarkably close to the expected 0.968 of an ideal centric system. No systematic absences were found, so the lowest symmetry centrosymmetric space group $P\bar{3}$ was chosen for an initial solution. The positions of the heavier atoms (Mg and Co) were determined using intrinsic phasing (SHELXT³²). A combination of least-squares refinement and difference Fourier maps (SHELXL³³) located substantial electron density (~ 50 e⁻) at around 0.4 Å from the Co 3f site, which was added as another Co atom in a 6g site and constrained such that the total occupancies of the 3f site and the two adjacent, symmetry-related instances of the 6g site sum to unity. B was found to be located in another 6g site, forming triangles with an unrealistically short B–B separation of 0.82 Å; the occupancy factor for the B site was constrained to $1/3$ to avoid unrealistically short bond distances.

Further analysis of the atomic coordinates suggested that certain atomic sites are located close to what would be a special site in a space group of higher symmetry. Therefore, the structure was solved in supergroups of $P\bar{3}$. The coordinates (0.00010, 0.49987, *z*) of the Co2 site in the $P\bar{3}$ space group are close to a 6i site (0, 1/2, *z*) in *P*6/*m*, a group where a mirror plane exists perpendicular to the *c*-axis. Refined coordinates of Co2 in these two solutions were not found to differ within the standard deviation (see Table S1). Additionally, the *z*-coordinate of the B site in $P\bar{3}$ does not differ within standard deviation from 0, resulting in a 6j (*x*, *y*, 0) site in *P*6/*m*. Furthermore, the coordinates of the boron site were found to be very close to (*x*, 2*x*, 0), suggesting the group *P*6/*mmm* where these coordinates constitute a special 6l site, as a consequence of additional mirror planes containing the *c*-axis in *P*6/*mmm*. In all cases, the refined atomic coordinates and relative occupancies do not differ between solutions within standard deviations. The *P*6/*mmm* solution yielded the lowest *R* values while the goodness-of-fit increased slightly since this refinement was performed against fewer independent data owing to the higher symmetry. Therefore, the highest symmetry group *P*6/*mmm* was chosen (see Table S1 for a comparison of atomic coordinates and occupancies for solutions in all three groups).

In the final stages of refinement, anisotropic harmonic displacement parameters (ADP) were refined for Co and Mg, with Co1 and Co2 ADP constrained to be identical at all stages of the refinement. High-angle data ($2\theta > 85^\circ$) were eliminated using the command OMIT –2 85 due to the low signal-to-noise ratio. A free refinement of the site occupancy of B site was attempted but resulted in occupancy of 34(1)%, which implies statistically possible cases of an unreasonably short B–B distance of 0.825 Å, although its ADP value remained reasonable. Therefore, for the final refinement, B site occupancy was fixed at 1/3. Cell parameters and atomic sites with occupancies and isotropic thermal parameters are listed in Table 1;

experimental parameters, crystallographic details, refinement statistics, and anisotropic thermal parameters are given in Tables S2 and S3. All crystal structures are plotted using the VESTA 3 visualization software.³⁴ Further details of the crystal structure refinement can be obtained from the Inorganic Crystal Structure Database (ICSD) from FIZ Karlsruhe–Leibniz Institute for Information Infrastructure (www.fiz-karlsruhe.de) by quoting the CSD 2369299 deposition number at www.ccdc.cam.ac.uk/structures.

Temperature-Resolved In Situ Powder X-ray Diffraction. High-temperature in situ X-ray diffraction was used to investigate the formation mechanism and determine the synthesis temperature of MgCo₃B₂. To track in situ formation of MgCo₃B₂, data were collected at beamline 17-BM (Advanced Photon Source, Argonne National Laboratory) at wavelength $\lambda = 0.24110$ Å between 298 and 1172 K, at a ramp rate of 20 K/min. The powders of magnesium hydride, cobalt, and boron taken in a 1:1:1 molar ratio were ball-milled for 18 min and sealed in a silica capillary (0.5 mm inner diameter, 0.7 mm outer diameter) under vacuum. The capillary was filled to approximately 1 cm with powder, and sealed with a length of at least 5 cm. In our experience, this provides adequate head space to prevent overpressurization and capillary explosion due to buildup of hydrogen gas from the hydride precursor. The sealed capillary was then mounted into a secondary shield capillary (0.9 mm inner diameter, 1.1 mm outer diameter) located on a sample stage equipped with two resistive microheaters and a thermocouple set as close to the measurement areas as possible.³⁵ The vertical setup was used for in situ data collection.³⁶ The uncertainty in the temperature measurement increases with temperature and is estimated to be ± 30 K above 873 K. Rietveld analysis was performed on selected patterns using GSAS-II.³⁰

Temperature-Resolved X-ray Diffraction of Prereacted MgCo₃B₂. To study decomposition and thermal stability of MgCo₃B₂, a sample containing MgCo₃B₂ as a major phase synthesized from elemental Mg was used. Data were collected at beamline 28-ID-2 (National Synchrotron Light Source II, Brookhaven National Lab) at wavelength $\lambda = 0.1824$ Å between 298 and 1169 K. A capillary was filled with approximately 2.5 cm of powder and sealed with a length of 3 cm. The sample was mounted at the beamline in a horizontal setup and heated in a similar manner to the 17-BM measurement using a sample stage with two resistive heaters and a thermocouple.³⁵ The uncertainty in the temperature measurement increases with temperature and is estimated to be ± 30 K above 873 K.

DFT Calculations. Density functional theory (DFT) calculations were performed using VASP³⁷ employing the Perdew–Burke–Ernzerhof (PBE) generalized gradient approximation (GGA) exchange-correlation functional³⁸ and the projector augmented wave (PAW) method.³⁹ A plane-wave-basis set with a kinetic energy cutoff of 520 eV was used. The convergence thresholds were 10^{-5} eV for electronic self-consistency and 0.01 eV Å⁻¹ for structural optimization. The Brillouin zone was sampled by the Monkhorst–Pack scheme⁴⁰ with a *k*-point grid of $2\pi \times 0.033$ Å⁻¹ in the structural optimization and with a denser *k*-point grid of $2\pi \times 0.022$ Å⁻¹ in the static calculation. The formation energies of MgCo₃B₂ in the CeCo₃B₂, MgNi₃B₂, and ZrCo₃B₂ structure types were obtained from spin-polarized calculations.

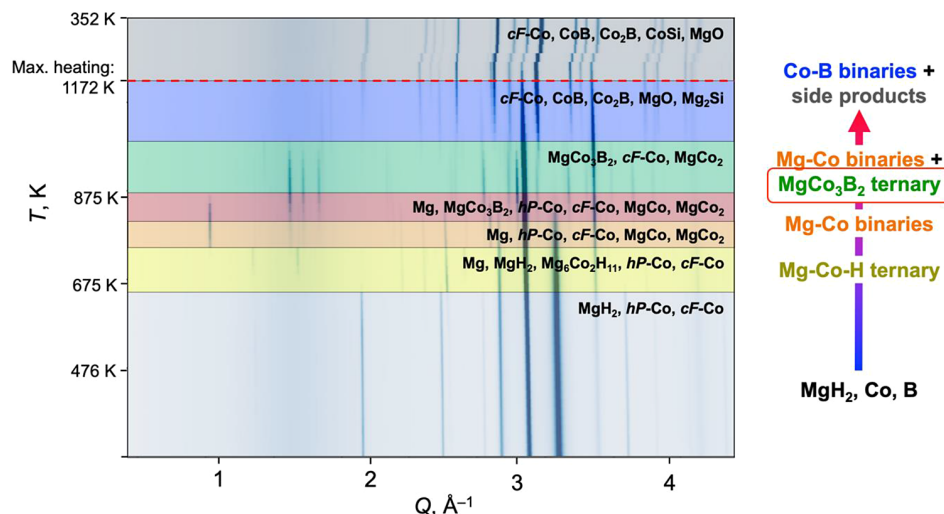


Figure 1. Temperature-resolved in situ powder X-ray diffraction of a precursor mixture containing powdered MgH₂, Co, and B in a 1:1:1 ratio. Each horizontal section is a PXRD pattern where darker shading indicates higher relative intensity. The schematic on the right illustrates the proposed formation mechanism of MgCo₃B₂. Precursors MgH₂ and Co initially react to form a ternary hydride Mg₆Co₂H₁₁ and elemental Mg, which then react with excess Co to form two Mg–Co binary compounds. Next, the ternary boride MgCo₃B₂ forms at 816 K and is stable up to 1016 K, where it transforms into Co–B binary compounds and products of side reactions with the silica capillary. The cobalt precursor consisted of hexagonal (*hP*-Co) and cubic (*cF*-Co) allotropes, and the hexagonal allotrope was observed to convert into the high-temperature stable face-centered cubic allotrope above 900 K. Data were collected at beamline 17-BM APS ANL at wavelength $\lambda = 0.24110 \text{ \AA}$.

Differential Scanning Calorimetry. DSC measurements were carried out using a Netzsch 404 F3 Pegasus Differential Scanning Calorimeter on a powdered sample sealed under vacuum in a silica ampule. Thermal stability was investigated by heating to 1173 K and cooling to 373 K, both at a rate of 10 K min^{-1} .

Magnetic Property Measurements. Magnetization measurements were performed on a polycrystalline powder sample of MgCo_3B_2 synthesized from magnesium hydride, sealed in a glass EPR tube under vacuum to prevent oxidation and sample loss. This sample was found to contain 83 wt % MgCo_3B_2 from Rietveld refinement of laboratory PXRD with impurities of metallic Mg and antiperovskite $\text{MgCo}_3(\text{B},\text{C})$. A Quantum Design MPMS 3 SQUID magnetometer was used for measurements of *dc* magnetization as a function of temperature between 5 and 300 K at 0.1, 3.5, and 7 T fields, isothermal field-dependent magnetization up to 7 T at 5 and 300 K, and *ac* susceptibility (with 1 Oe *ac* field) at 1000 Oe *dc* bias field between 2 and 50 K and frequencies of 10, 100, and 1000 Hz.

■ RESULTS AND DISCUSSION

In Situ Synthesis of MgCo₃B₂. Unlike the systems A-Ni—B (A = Mg—Ba) where several ternary compounds have been reported with a variety of compositions and structures, no ternary compounds have yet been reported for Co-containing systems, including the Mg—Co—B system. To quickly screen for a novel ternary phases, an *in situ* synchrotron X-ray powder diffraction experiment was performed using a 1:1:1 molar ratio of MgH₂, Co, and B powders. In an *in situ* synthesis reaction, powder X-ray diffraction (PXRD) patterns are collected incrementally during heating (and cooling) of unreacted precursors sealed in a silica capillary to reveal hidden phase transformations. The PXRD data from the *in situ* experiment are depicted as a waterfall plot in Figure 1, a stack of PXRD patterns where a darker shading corresponds to higher relative diffraction intensity. The patterns are arranged from bottom to top, so moving up the y-axis represents slow heating followed by fast cooling. A waterfall plot is a convenient way to show all the PXRD data from an *in situ* experiment in one graphic, and effectively conveys qualitative information about phase trans-

formations and identities. However, due to the conversion of peak intensity into gradations in shading in the waterfall plot, small peaks are not always discernible in such a representation, especially if they are found in a region with many other peaks nearby, so minor phases are easily overlooked. Therefore, it is essential to carefully inspect each PXRD pattern in succession and perform a Rietveld refinement whenever peaks appear or disappear. The phase fractions determined by such a set of refinements for this *in situ* data set are listed in [Table S4](#). Phase analysis on representative PXRD patterns from each region indicated in [Figure 1](#) is shown in [Figure S1](#). While most of the PXRD patterns for the Mg–Co–B experiment consisted of peaks that could be matched to known elements or binary phases, two regions (colored yellow and green in [Figure 1](#)) were found to be of particular interest; representative PXRD patterns from these regions are analyzed in [Figure 2](#).

The first transformation that takes place is the decomposition of MgH_2 to elemental Mg, accompanied by the formation of the known ternary hydride $\text{Mg}_6\text{Co}_2\text{H}_{11}$. Early reports of this phase differ as to its exact composition and symmetry; a neutron diffraction study of the deuterated compound established the composition above and an orthorhombic structure in space group $Pnma$.⁴¹ The initial reports describe heating under ~ 5 MPa of hydrogen to produce this phase.^{41,42} In the synthesis utilized here, decomposition of the MgH_2 precursor in the sealed tube would have afforded the hydrogen pressures needed to form the phase. This ternary hydride appears to be stable over a relatively narrow temperature range of 696–756 K, above which it gives way to two different Mg–Co binary compounds: MgCo ⁴³ and MgCo_2 .⁴⁴ Peaks for the ternary hydride phase are indicated with gray boxes in Figure 2a.

Between 816 and 1016 K, a set of peaks is observed that cannot be matched to known phases composed of Mg, Co, B, and H. The locations and intensities of these peaks resemble those of MgNi_3B_2 , as shown in Figure 2b. Although some of these peaks overlap with or are nearby those of MgCo_2 , a

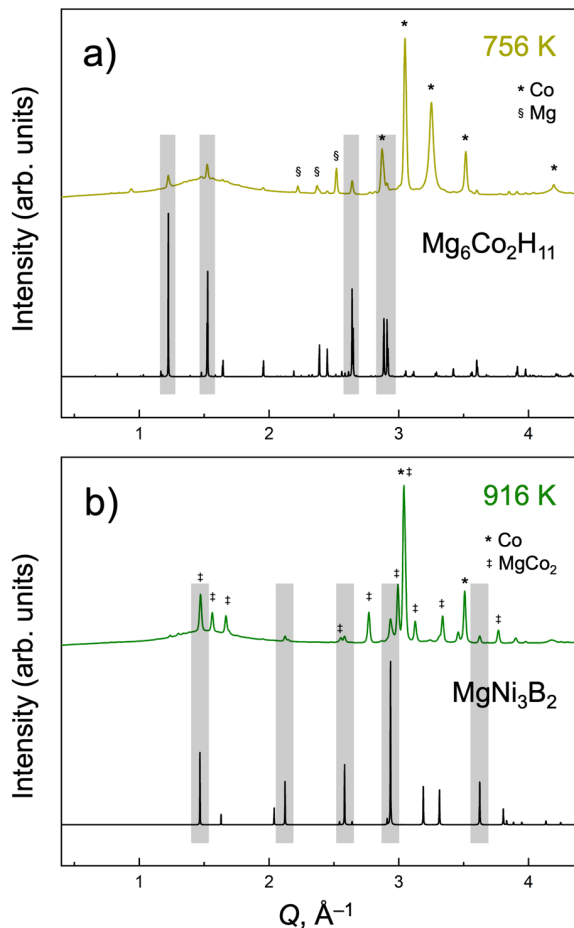


Figure 2. Selected PXRD patterns from an in situ reaction of MgH_2 , Co, and B. Top patterns are measured data at the temperature indicated; bottom patterns are theoretical patterns for the specified phase. The gray boxes highlight the major peaks of the phases of interest and serve as a guide to the eye. (a) in PXRD pattern at 756 K, small peaks corresponding to the $Mg_6Co_2H_{11}$ phase are highlighted; (b) PXRD pattern at 916 K contains small peaks that do not match any known phases composed of Mg, Co, B, and/or H but are quite close to predicted peaks for $MgNi_3B_2$. Both patterns feature large peaks for major phases as indicated with symbols, and other small peaks for minor impurity phases. For a more thorough phase analysis of these and other representative patterns, see Figure S1.

major phase at this temperature, Rietveld analysis clearly indicated unaccounted peak intensity at the locations indicated by gray boxes in Figure 2b. This prompted DFT evaluation of the phase with composition $MgCo_3B_2$ in the $MgNi_3B_2$ structure, which revealed a favorable formation energy of -37.7467 eV/f.u. for this potential compound. Interestingly, $MgCo_3B_2$ is not identified as a stable compound in available databases of high-throughput materials predictions.^{45–48} In the in situ experiment, the ternary boride persists up to 1016 K, although its weight fraction never exceeds 12.4 wt %, derived from Rietveld analysis of the PXRD pattern measured at 916 K. Both $MgCo_3B_2$ and $MgCo_2$ cease to be observed above 1016 K, a range in which Co–B binary compounds prevail, as well as Mg_2Si , $CoSi$, and MgO formed by side reactions with the silica capillary walls.

In summary, the in situ synthesis experiment strongly suggests the existence of a new ternary boride phase with composition $MgCo_3B_2$, in analogy to the known phase

$MgNi_3B_2$. Peaks for this compound are only observed in the range 816–1016 K, suggesting that this phase becomes less energetically favorable with respect to Co–B binary compounds at $T > 1000$ K and providing insight into the temperature range suitable for ex situ synthesis. The observed set of reactions comprising the formation and decomposition of this phase is quite complex: MgH_2 and Co react to form the ternary hydride phase $Mg_6Co_2H_{11}$, then excess Co reacts with this phase or Mg from the decomposition of MgH_2 to form $MgCo$ and $MgCo_2$ binary phases. Above 816 K, the first boride is observed in the form of ternary $MgCo_3B_2$, which may be the product of the reaction of $MgCo$ with excess Co and B, or of the three constituent elements individually. Above 1016 K, this compound reacts with the capillary walls to form MgO and Mg_2Si , leaving behind CoB and Co_2B . Complete elucidation of these structural transformations was only possible after careful Rietveld analysis of successive PXRD patterns accompanied by manual searching of several crystal structure databases.^{49–51} Attempts to automate this process are highly prone to error and often lead to misidentification of major phases while minor components are overlooked entirely.⁵²

Ex Situ Synthesis of $MgCo_3B_2$. Guided by insight from the in situ diffraction experiment, ex situ synthesis of $MgCo_3B_2$ was initially carried out using magnesium hydride and elemental cobalt and boron precursors. A loading composition of $MgH_2:Co:B = 1.8:3:2.4$ was chosen in analogy to the optimized composition of $LiH:Ni:B = 1.7:3:2.4$ used for $LiNi_3B_{1.8}$, a closely related phase (vide infra) that has been successfully synthesized using the hydride route.¹³ In our experience, an excess of alkali/alkaline-earth element is often found to be necessary to stabilize a given phase; in some cases, the excess may exceed 2-fold. Unlike $LiNi_3B_{1.8}$, however, which forms in the highest purity after a short dwell at 1173 K followed by a longer dwell at 1023 K, in situ diffraction suggests that $MgCo_3B_2$ is a less favored phase at temperatures above 1023 K. This was confirmed by initial attempts at ex-situ synthesis, where an optimal synthesis temperature of 1023 K was determined. During the synthesis optimization, binary $MgCo_2$ was frequently produced as a competing phase, particularly when decreasing the initial amount of magnesium and when starting from elemental magnesium. This aligns with in situ evidence, which shows peaks for $MgCo_2$ across the entire range over which $MgCo_3B_2$ is observed to be stable. In general, while $MgCo_3B_2$ is observed to be formed from reactions spanning a wide range of compositional phase space and heating profiles, Mg–Co and Co–B binaries tend to prevail when the Mg:Co ratio is decreased below 1.8:3, and Co_2B is observed to form more readily above 1023 K.

To eliminate the possibility that this new compound might be a hydride-stabilized phase, attempts were made to synthesize it from elemental magnesium rather than magnesium hydride. This proved to be successful, although about 5% excess of magnesium was required when compared to the loading composition optimized for reaction from magnesium hydride. One of the advantages of the hydride route is that it permits precise control of precursor stoichiometry. Working from an elemental magnesium precursor meant that turnings of magnesium metal had to be added to ball-milled cobalt and boron, and the actual Mg:Co ratio usually deviated from the desired 2:3 by up to 0.05 with respect to 3 equivalents of cobalt. While this may not seem significant, it was found that decreasing the Mg:Co ratio even to 1.9:3, a difference of 0.1 relative to 3 equivalents of cobalt,

resulted in the formation of MgCo_3B_2 as the major phase with little evidence of the ternary phase.

Growing crystals of MgCo_3B_2 suitable for single-crystal X-ray diffraction proved to be challenging. Initial attempts involved the same preparation as described above for the synthesis of polycrystalline MgCo_3B_2 from elemental magnesium with an extended dwell at 1073 K and slow cooling to 673 K. Then, a magnesium flux (3 equiv with respect to MgCo_3B_2), as well as $\text{MgCl}_2/\text{NaCl}$ eutectic and MgCl_2 salt fluxes, were attempted. Each of these attempts resulted in crystal sizes too small for single-crystal X-ray diffraction in a laboratory setup. It was only when eliminating the flux and including an initial heating step at 1173 K for 48 h, a slow cool to 1073 K, and an extended dwell at that temperature for 100 h before the slow cooling step that the crystals of larger size began to form. However, even this optimized profile yielded only very small crystals ($\approx 10 \mu\text{m}$ across) of irregular shape, most of which were comprised of multiple crystalline domains. A suitable crystal of dimensions $5 \times 5 \times 15 \mu\text{m}$ was eventually isolated and used for data collection. Interestingly, Manfrinetti et al. in their report on MgNi_3B_2 do not utilize a flux for crystal growth but found that extended dwelling at 1173 or 1223 K gave a sample from which a crystal (measuring $40 \times 40 \times 110 \mu\text{m}$) could be isolated.²⁴

MgCo₃B₂ Crystal Structure Solution. From the initial indications of a new Mg–Co–B phase from in situ PXRD, it was apparent that the structure of this phase is closely related to that of MgNi_3B_2 , whose structure and relation to other structure types have been previously discussed at length. In summary, the MgNi_3B_2 structure type is a variant of the CeCo_3B_2 structure type ($P6/mmm$), which itself is a ternary ordered variant of CaCu_5 .²⁴ In the CeCo_3B_2 structure, B is six-coordinate by Co, forming BCo_6 trigonal prisms that share edges along the c -direction and create hexagonal cavities filled by chains of Ce atoms along the c -direction. Ce and B atoms lie within the plane $z = 0$, while Co atoms occupy $3c$ sites and form a perfect Kagomé network in the $z = 1/2$ plane as dictated by the mirror symmetry.⁵³ In MgNi_3B_2 ($P6_{4}22$), mirror symmetry perpendicular to c is removed, which allows for a slight distortion of the Kagomé network of Ni atoms, and the 6-fold proper rotation axis is replaced by a screw axis, which allows B atoms to be slightly displaced from their special site ($1/3, 2/3, 0$) to form dimers (B–B distance = 1.876 \AA). The presence of this 6_4 screw axis also creates a 3-fold expansion of the unit cell along c , which in turn gives rise to additional reflections with indices $l \neq 3n$. Another variant of this structure is found in the case of ZrCo_3B_2 , which adopts a rhombohedral cell ($R\bar{3}$) and also features a rumped Kagomé network of Co atoms as well as B dimers.⁵⁴ However, since the group $R\bar{3}$ is not chiral, its symmetry dictates that the B dimers in adjacent layers be related by both 3_1 and 3_2 screw axes, while in the $P6_{4}22$ structure, only a 3_1 axis is present. Additionally, a monoclinic variant of the CeCo_3B_2 structure type has been reported for many $RT_3\text{B}_2$ compounds, where T is a $4d$ or $5d$ element. This structure has the prototypical formula ErIr_3B_2 and is only very slightly distorted from the CeCo_3B_2 type; the cell is nearly orthorhombic with $\beta \approx 90^\circ$. The relationship between the unit cells of these structures are discussed in more detail in the Supporting Information; representative structures are plotted in projection onto the ab -plane in Figure 3.

Refinement of single-crystal XRD data was carried out in a hexagonal cell with $a = b = 4.883 \text{ \AA}$, $c = 2.926 \text{ \AA}$, equivalent to the CeCo_3B_2 cell. Further analysis (see Experimental) strongly

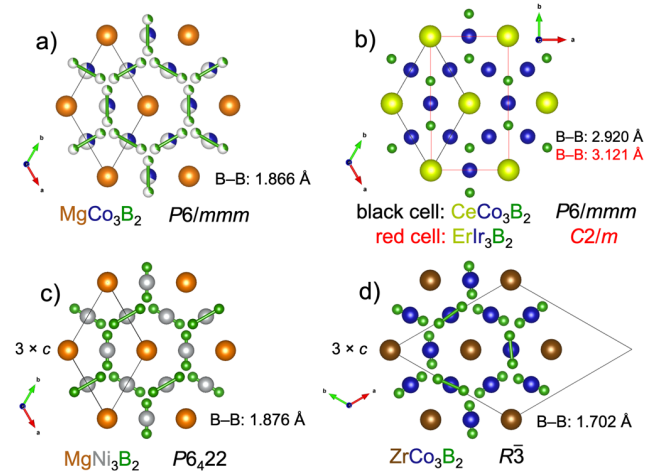


Figure 3. Projections along c of four different structure types derived from CeCo_3B_2 : (a) MgCo_3B_2 (this work), disordered variant of CeCo_3B_2 ; (b) CeCo_3B_2 and ErIr_3B_2 featuring isolated boron atoms rather than dimers; (c) MgNi_3B_2 , chiral variant of CeCo_3B_2 featuring a 6_4 screw axis and $3 \times c$ unit cell; and (d) rhombohedral ZrCo_3B_2 in centrosymmetric space group $R\bar{3}$ with conventional hexagonal setting. For relations between the cells plotted here, please refer to the Supporting Information.

suggested a centrosymmetric space group. After attempts in $P\bar{3}$, $P6/m$, and $P6/mmm$, the highest symmetry $P6/mmm$ was chosen. Structure solution using intrinsic phasing (SHELXT) located Mg and Co atoms in the same sites as Ce and Co in CeCo_3B_2 . During least-squares refinement coupled with difference Fourier maps, significant electron density at around 0.4 \AA from Co was refined as a Co split site; B atoms were found to occupy a 6-fold site with occupancy factor constrained to $1/3$. The final refinement with anisotropic atomic displacement parameters (ADPs) for Mg and Co converged to R_1 (all data) = 0.0248, wR_2 = 0.0449, and $\text{GoF} = 1.117$. Details on the process of refining the crystal structure are provided in the Experimental section; unit cell parameters, atomic coordinates, site occupancy factors, and atomic displacement parameters are given in Table 1. Anisotropic thermal parameters and additional refinement details can be found in Tables S1–S3.

MgCo₃B₂ Crystal Structure Description. The refined structural model with disordered Co and B sites as well as an average structure are shown in Figure 4a. In the average structure, which is equivalent to the ordered CeCo_3B_2 structure, Co atoms occupy a 3-fold site ($3g$) and B atoms occupy a 2-fold site ($2c$). In MgCo_3B_2 , what would be one Co atom in the CeCo_3B_2 structure is split along the z -axis into three positions, each with roughly $1/3$ occupancy: one Co1 atom, located in a $3g$ site with z -coordinate $0.5c$, and two Co2 atoms, located in a $6i$ site with z -coordinate $(0.5 \pm 0.118)c$. The separation between Co atoms at these two sites is $0.118c$ or 0.345 \AA , so only one of the three positions can be occupied at a time. Likewise, what would be one B atom in the CeCo_3B_2 structure at a $2c$ site is shifted by 0.475 \AA within the plane $z = 0$ into a $6l$ site. The higher multiplicity of this site would lead to the formation of triangles of B atoms separated by 0.822 \AA , so the occupancy of this site was constrained to $1/3$, which makes such unreasonably short B–B contact statistically impossible.

B–B Interatomic Separations and Environment. In the CeCo_3B_2 -like ordered structure of MgCo_3B_2 , Co atoms form

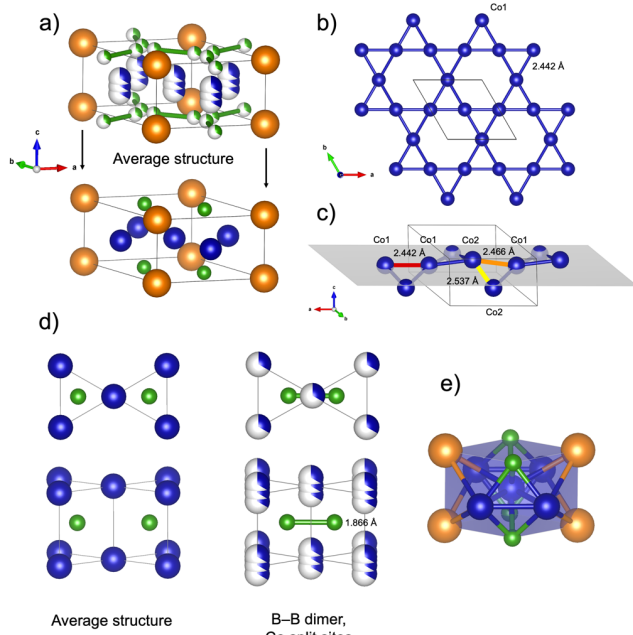


Figure 4. Structure of MgCo_3B_2 . (a) Comparison of the disordered model of MgCo_3B_2 with split Co and B sites and the average structure obtained by eliminating Co2 and moving B from a split 6l site to a fully occupied 2c site; (b) the idealized Kagomé network of only Co1 atoms viewed along the *c* axis; (c) a more realistic scenario in which interactions between neighboring Co atoms with differing *c*-coordinate are considered, with each of the three distinct bond distances outlined in a different color; (d) comparison of B–B interatomic separations and BCo_6 coordination polyhedra between the average structure and the disordered structure with Co and B split sites and B–B dimers; and (e) capped rhombic prismatic geometry of 12-coordinate Co in the average structure.

trigonal prisms that share edges along the *c*-axis. Isolated B atoms lie in the center of these prisms, and the prisms themselves connect to form hexagonal channels running along the *c*-axis that would contain Mg atoms. In the disordered structure, partial occupancy of the Co split sites causes the BCo_6 prisms to become distorted compared to the idealized geometry manifested in CeCo_3B_2 . Additionally, the B atoms are displaced from the center of the prisms at $(\frac{1}{3}, \frac{2}{3}, 0)$ to bond through the shared edge of two adjacent prisms and form a B–B dimer (Figure 4d) with a separation of 1.870 Å. This is remarkably close to the B–B distance in MgNi_3B_2 of 1.876 Å, but longer than the B–B separation of 1.702 Å in ZrCo_3B_2 . Importantly, this motif is part of what distinguishes the structures of MgNi_3B_2 and ZrCo_3B_2 from the higher-symmetry CeCo_3B_2 structure adopted by all of the RCO_3B_2 compounds.¹³

Co–Co Kagomé Network. In the CeCo_3B_2 structure type, the substructure of Co atoms forms a perfect flat Kagomé network (Figure 4b). In MgCo_3B_2 , the random distribution of Co across two split sites leads to a rumpling of the Kagomé network above and below the plane at *z* = 0.5*c*. In the case of MgCo_3B_2 , for an idealized Kagomé network consisting only of fully occupied Co1 atoms, the distance between adjacent Co atoms would be 2.442 Å in all cases (Figure 4b). In the refined disordered model, three Co–Co bond distances are possible (Figure 4c). The first bond distance of 2.442 Å (shown in red in Figure 4c) occurs in the case of two adjacent Co atoms with the same *z*-coordinate, i.e., either between adjacent Co1 or adjacent Co2 atoms. The second bond distance is the one

found between a Co1 atom and a neighboring Co2 atom; these atoms will necessarily differ in their *z*-coordinate by 0.118*c*, leading to a greater separation of 2.466 Å (shown in orange in Figure 4c). Finally, a Co2 atom sitting above the plane *z* = 0.5*c* (shown in Figure 4c) may be connected to a Co2 atom sitting below this plane; in this case the *z*-coordinates of these two atoms differ by 0.236*c*, and the resulting separation is the longest at 2.537 Å (shown in yellow in Figure 4c). Each of these possible distances is reasonable for a Co–Co metallic bond: the Co–Co separation in metallic Co is 2.513 Å in the case of the cubic allotrope and 2.503 Å in the case of the hexagonal allotrope, while in Co_2B an even closer separation of 2.426 Å is observed. For in-depth discussion of coordination environments of Co and B, please refer to Figures S2 and S3 and the associated discussion.

To determine whether the observed disorder in the small cell is a superposition of multiple Co sites exhibiting long-range order (creating a supercell or incommensurately modulated structure) or short-range order (resulting in diffuse scattering), precession images of reconstructed reciprocal lattice planes were analyzed (Figure S4). Although a number of faint streaks and spots were observed in reciprocal planes *h*0*l*, 0*k**l*, and *h**h**l*, they do not form any regular patterns that would be suggestive of a superstructure or of higher-dimensional symmetry, nor are the observed reflections elongated in any direction, which would be indicative of diffuse scattering. These images provide compelling evidence that the primitive hexagonal cell chosen for single-crystal refinement is best suited for the MgCo_3B_2 structure. The case of $\text{Mg}_2\text{Rh}_{1-x}\text{B}_{6+2x}$ is in some ways akin to the structure in question: both MgCo_3B_2 and $\text{Mg}_2\text{Rh}_{1-x}\text{B}_{6+2x}$ are disordered variants of an ordered *R*–T–B compound (*viz.*, CeCo_3B_2 and Y_2ReB_6) where site splitting is observed without indications of a superstructure. In the case of $\text{Mg}_2\text{Rh}_{1-x}\text{B}_{6+2x}$, the disordered structure in a primitive orthorhombic cell features a position split between Rh and a B dimer, and electron diffraction images were used to rule out the possibility of a superstructure.⁵⁵

Rietveld Analysis of HR-PXRD for MgCo_3B_2 . To help confirm the validity of the structural model refined from single-crystal X-ray diffraction, a Rietveld refinement was attempted using high-resolution PXRD data. The result was compared to that of similar refinements using structural models for MgNi_3B_2 , ZrCo_3B_2 , and CeCo_3B_2 with appropriate atomic substitutions and unit cell parameter adjustments (Figures S5–S7, Tables S5 and S6). For these refinements, known impurity phases were added, and all unit cell parameters, background coefficients, scale factor, and phase fractions were refined. Because the models for MgNi_3B_2 and ZrCo_3B_2 feature a superstructure, additional peaks are predicted that are lacking in the experimental pattern (marked in Figures S5 and S6). The structure for CeCo_3B_2 adopts the same unit cell as the model for MgCo_3B_2 refined from SCXRD data with no additional diffraction peaks. However, the CeCo_3B_2 model does not accurately describe the observed peak intensities since there are multiple peaks with a significant disparity in intensity between the CeCo_3B_2 model and the observed pattern (marked in Figure S7). Only the disordered CeCo_3B_2 -like structure obtained from SCXRD can correctly fit the powder diffraction data; alternate, ordered models either do not correctly model observed peak intensities or give rise to extraneous peaks as a result of a superstructure.

After refining several sample parameters, including phase fractions of impurity phases, Rietveld refinement of the SCXRD model yielded a wR value of 0.038 with MgCo_3B_2 comprising 89.15 wt % of the sample. Visual inspection of the observed and predicted profiles reveals an excellent fit (Figure S8), confirming that MgCo_3B_2 has been prepared in high yield and validating the structural model from SCXRD. Cell parameters from the refinement, together with the refined weight percent of identified impurity phases, are listed in Table S6.

Comparison of MgCo_3B_2 with Related Structure Types. In Figure S9, bond lengths and interatomic separations of MgCo_3B_2 and MgNi_3B_2 ²⁴ are compared. In all cases, distances between comparable atoms are remarkably similar. The only essential difference between the two types is that for the chiral MgNi_3B_2 structure, Ni atoms with the same z -coordinate are never found adjacent to each other in the rumpled Kagomé network, while for MgCo_3B_2 a Co1–Co1 or Co2–Co2 bond of 2.442 Å is statistically possible due to the disorder. This bond distance is slightly on the shorter side but not unreasonable for both Co–Co and Ni–Ni bonding.

It may well be asked why MgCo_3B_2 does not simply adopt one of the ordered structure types known for other Mg- or Co-containing analogs. RCO_3B_2 ternary compounds have been reported for $R = \text{Sc}, \text{Y}, \text{Ce}, \text{Sm}, \text{Gd}, \text{Tb}, \text{Dy}, \text{Ho}, \text{Er}, \text{Tm}, \text{Yb}$, and Lu , all of which are reported to crystallize in the prototypical CeCo_3B_2 structure type featuring isolated B atoms rather than dimers.^{53,56} The R metals in RCO_3B_2 have +3 as a common oxidation state, while Mg exhibits a +2 oxidation state. Supposing that electron transfer occurs from M to the T–B framework in $MT_3\text{B}_2$ compounds, R can donate up to 3 electrons in RCO_3B_2 (for all R except Ce), so B atoms tend to isolate from each other. On the other hand, in MgCo_3B_2 , MgNi_3B_2 , and $\text{LiNi}_3\text{B}_{1.8}$, the electropositive element only contributes up to one or two electrons to the T–B framework, so B atoms are more prone to form dimers to share electrons. For ZrCo_3B_2 , the nominal oxidation state Zr^{4+} implies strong electron donating ability, which should lead to isolated B atoms. However, Zr has lower electron-donating ability compared to the rare-earth elements because of a stronger tendency to form localized covalent bonds. This is confirmed by Bader charge analysis on MgNi_3B_2 and ZrCo_3B_2 , indicating $\text{Mg}^{1.54+}$ and $\text{Zr}^{1.53+}$ Bader charges, respectively (see Table S7). Therefore, in terms of charge transfer, Zr behaves much like Mg in ZrCo_3B_2 , so with fewer electrons available to the T–B framework, the formation of B–B dimers is observed.

DFT Assessment of MgCo_3B_2 Formation Energy. Since electronic structure calculations for compounds exhibiting structural disorder are not straightforward, the formation energies for composition MgCo_3B_2 were obtained for the three ordered structure types shown in Figure 3 (CeCo_3B_2 , MgNi_3B_2 , and ZrCo_3B_2). The DFT calculations were first performed using unrelaxed structures where unit cell parameters $a = 4.89240$ Å and $c = 2.93113$ Å (as refined from HR-PXRD data) were adapted to the three structure types of interest (using the relationships listed in the Supporting Information) while atomic coordinates were taken from reported models obtained using SCXRD for CeCo_3B_2 , MgNi_3B_2 , and ZrCo_3B_2 .^{24,53,54} In addition, formation energies were calculated after DFT relaxation was performed for all three models (Table 2). Before relaxation, the MgNi_3B_2 structure type was calculated to be the most energetically favorable, but after relaxation, the ZrCo_3B_2

Table 2. DFT Formation Energies for MgCo_3B_2 with and without DFT Relaxation in Three Different Structure Types^a

structure type	magnetic ordering	formation energy (unrelaxed) (eV/f.u.)	formation energy (relaxed) eV/f.u.
CeCo_3B_2	NM ^b	-37.5675	-37.7282
MgNi_3B_2	NM ^b	-37.7142	-37.7510
	AFM		-37.7485
	FM		-37.7467
ZrCo_3B_2	NM	-37.4107	-37.7671
	FM ^b		-37.7676

^aSpin-polarized DFT calculations reveal various relaxed structures with different magnetic order. NM = non-magnetic (paramagnetic or diamagnetic), FM = ferromagnetic, AFM = antiferromagnetic.

^bGround state.

structure type was found to be slightly more favorable, although the formation energies for all three structure types are much closer after relaxation. For the cases of MgNi_3B_2 and ZrCo_3B_2 , the cell volume decreased slightly; this is expected since DFT calculations model energetic behavior at 0 K. The MgNi_3B_2 -type structure did not change substantially with the DFT relaxation, as evinced by the relatively slight change in energy during relaxation. The ZrCo_3B_2 -type structure changed most significantly after the relaxation. Before relaxation, the B dimers displayed a bond distance of 1.713 Å and were twisted slightly out of the *ac*-, *bc*-, and other symmetry-related planes. After relaxation, the B atoms were found to lie within these planes, which allowed the structure to be described in higher symmetry group $\bar{R}\bar{3}m$ (#166) as determined using FIND-SYM,^{57,58} and the B–B distance increased to 1.874 Å, much closer to the experimental value of 1.870 Å (Figure S10). A previous computational study also found that DFT optimization caused the experimental $\bar{R}\bar{3}$ structure of ZrCo_3B_2 to relax to higher-symmetry $\bar{R}\bar{3}m$ model.⁵⁹

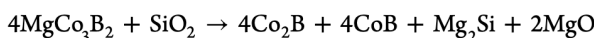
After relaxation, the CeCo_3B_2 -type structure is the least energetically preferred. The substantial change in energy between unrelaxed and relaxed structures is due to a change in unit cell parameters: a increases from 4.89240 to 5.08131 Å while c decreases from 2.93110 to 2.72590 Å, with a relatively constant unit cell volume (60.758 Å³ before vs 60.956 Å³ after relaxation). This leads to a relative increase in bond distances within a single layer while distances between atoms in different layers decrease in length. In particular, the Co–Co distance increases from 2.442 Å, the separation that would be observed in a perfect Kagomé network with experimental unit-cell parameters, to 2.541 Å, which is slightly longer than the longest possible Co2–Co2 distance in the disordered structure, namely 2.536 Å. The Co–B distances are reduced from 2.035 to 2.002 Å, slightly shorter than any of the realistic Co–B bonds in the disordered structure. For CeCo_3B_2 , the Co–Co distance is approximately 2.53 Å, and for other RCO_3B_2 compounds it ranges from 2.47 to 2.54 Å. This observation suggests that another reason MgCo_3B_2 does not adopt the ordered $P6/mmm$ structure displayed by all the RCO_3B_2 compounds is that a perfect Kagomé network of all Co atoms within the plane $z = 0.5$ would force the atoms to move apart to achieve an optimal separation of ~2.5 Å. This would lead to an increase in the a cell parameter which would be compensated by a decrease in the c parameter to maintain reasonable Mg–Co and Mg–B spacing, permitted by the smaller ionic radius of Mg compared to R. The unit-cell

distortion of the DFT-relaxed CeCo_3B_2 structure as well as its higher formation energy can be interpreted as suggesting that a flat network of Co atoms is not a favorable motif for MgCo_3B_2 .

Additionally, Bader charge analysis performed for DFT-relaxed MgCo_3B_2 in the MgNi_3B_2 and ZrCo_3B_2 structure types indicates effectively the same Bader charges for each atom type between the two structures. The charge assignment $\text{Mg}^{1.55+}(\text{Co}^{0.25-})_3(\text{B}^{0.39-})_2$ shows that Mg exists in a fairly ionic state, while Co donates a small amount of electron density to B, as would be expected based on electronegativity values. These charges are also comparable to those determined for the structures of the MgNi_3B_2 and ZrCo_3B_2 compounds themselves (see Table S7).

As noted above, materials featuring a Kagomé network are known to exhibit exotic electronic, magnetic, and quantum properties. In materials with well-separated two-dimensional Kagomé networks, the electronic band structures often exhibit Dirac cones and flat bands. For the disordered MgCo_3B_2 model as well as for the ordered, DFT-relaxed CeCo_3B_2 -type and MgNi_3B_2 -type, and ZrCo_3B_2 -type models of MgCo_3B_2 , the distance between Co atoms in adjacent Kagomé layers is similar to the distance between Co atoms within the Kagomé layer. In addition, the ratio between the shortest Co–Co separation within the Kagomé layer and the distance between a Co atom and its nearest neighbor (in this case, B) is 1.20. This means that the Co network in MgCo_3B_2 is classified as a “semi-interacting Kagomé” network in contrast to an “isolated Kagomé network” as manifested in compounds such as LiCo_6Ge_6 .²⁹ In the “semi-interacting Kagomé” networks, the Kagomé electronic bands are distorted by interactions with atoms not part of the Kagomé network, so characteristic Kagomé bands do not exist in these phases (Figures S11 and S12). Both nonspin-polarized and spin-polarized electronic structure calculations show metallic behavior for MgCo_3B_2 in both ordered structure types, with no indication of exotic band structure features characteristic of a compound containing an isolated Kagomé network.

Thermal Stability of MgCo_3B_2 . The high-temperature stability of a sample of MgCo_3B_2 sealed under vacuum in a capillary was evaluated by means of temperature-resolved synchrotron powder X-ray diffraction up to 1169 K (Figure 5a). Although trace impurities of Mg and Co_2B were present in the sample before heat treatment, their levels remained consistent up to 992 K, aside from the melting of Mg at 888 K. Above 992 K, the fraction of Co_2B gradually begins to increase and peaks for CoB emerge, indicating that decomposition of the ternary phase has begun. This is consistent with synchrotron PXRD of in situ formation of MgCo_3B_2 , where the ternary phase is observed to decompose into binary borides Co_2B and CoB above 1016 K. Presumably, in this case, Mg is also lost to a side reaction with the silica capillary, according to the reaction below:



However, the complete decomposition of MgCo_3B_2 does not occur during the fast heating up to 1169 K employed in the temperature-resolved synchrotron PXRD experiment, and the ternary phase remains the major phase upon cooling.

In addition, differential scanning calorimetry data were collected for a sample of MgCo_3B_2 sealed under vacuum (Figure 5b). The smooth curve suggests that gradual phase transformation takes place upon heating without substantial change in enthalpy within a narrow temperature range; this is

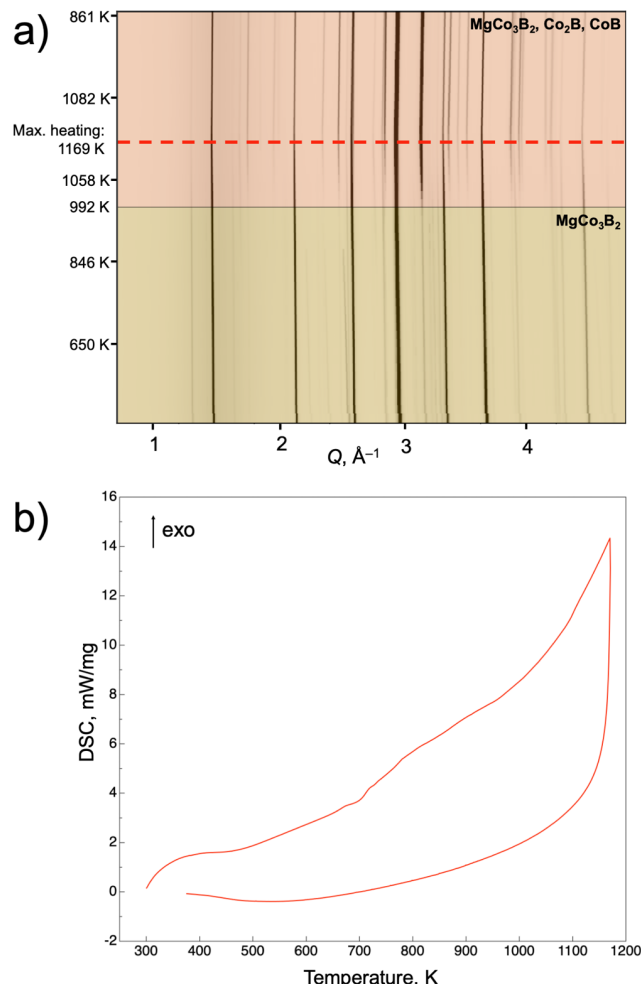


Figure 5. Thermal stability of MgCo_3B_2 . (a) Temperature-resolved PXRD of a prereacted sample of MgCo_3B_2 . Decomposition of the ternary phase into Co_2B and CoB begins at 992 K and continues gradually up to a maximum temperature of 1169 K. Initial and final PXRD patterns are compared with reference patterns for MgCo_3B_2 , CoB , and Co_2B in Figure S14. Data were collected at beamline 28-ID-2 NSLS-II BNL at wavelength $\lambda = 0.1824$. (b) Differential scanning calorimetry (DSC) measurement of MgCo_3B_2 sealed under vacuum up to 1173 K.

consistent with the formation of binary compounds observed in the temperature-resolved PXRD data, where the fractions of CoB and Co_2B increase smoothly from 992 K to the maximum temperature of 1169 K and then remain constant at roughly 20–30 wt % each upon cooling down to 861 K. Because the ternary phase persists even at high temperatures, a sequential refinement of unit cell parameters as a function of temperature was possible (Table S8). Linear fitting of the temperature dependence of a and c parameters and cell volume data between 500 and 1000 K (Figure S13) gives coefficients of thermal expansion (CTE) according to the following equations:

$$\text{CTE}(a) = \frac{da}{dT} \times \frac{1}{a} = 1.52(1) \times 10^{-5} \text{ K}^{-1}$$

$$\text{CTE}(c) = \frac{dc}{dT} \times \frac{1}{c} = 1.301(9) \times 10^{-5} \text{ K}^{-1}$$

$$\text{CTE}(V) = \frac{dV}{dT} \times \frac{1}{V} = 4.39(3) \times 10^{-5} \text{ K}^{-1}$$

To investigate the stability of the MgCo_3B_2 phase in air, a small amount (~ 10 mg) was placed in an open alumina crucible and heated to 973 K. Comparison of the PXRD patterns before and after heat treatment does not give any indication of decomposition of the ternary phase but rather reveals a reduction in the fraction of a Mg impurity present in the initial sample, most likely due to Mg evaporation and/or oxidation to form MgO . However, a longer dwell at 1173 K leads to the complete decomposition of the ternary phase into CoB and Co_2B , as well as MgO and CoO . PXRD patterns for these two tests are compared with that of the original sample in Figure S15.

Magnetic Properties of MgCo_3B_2 . A polycrystalline powder sample of MgCo_3B_2 synthesized from magnesium hydride was used for magnetic property measurements. According to Rietveld refinement of laboratory PXRD data for this sample, 83 wt % of the sample is composed of MgCo_3B_2 , with 7–10 wt % impurities of Mg and $\text{MgCo}_3(\text{B},\text{C})$. Measurements of temperature-dependent magnetization of MgCo_3B_2 at a low field of 1 kOe revealed a small positive magnetic susceptibility, suggesting bulk paramagnetism, with a non-Curie–Weiss temperature dependence (Figure S16). The presence of a small impurity (~ 0.1 wt %) of MgB_2 ($T_c = 39$ K) is inferred from a decrease in susceptibility below 36 K (Figure S16) and negative slope of magnetization at low field observed in the 5 K $M(H)$ measurement (Figure S17).⁸

At high fields, the dependence of magnetization on field, $M(H)$, is linear at both 5 K (Figure S17) and 300 K (Figure 6b), consistent with bulk Pauli paramagnetism of the sample. At 300 K, a rapid increase in magnetization at low fields suggests a saturation of a ferromagnetic impurity. By fitting the data above 35 kOe with a linear fit and extrapolating to zero field, the magnitude of the saturation at 5 K was found to be $9.2(2)$ emu/mol. Assuming this comes entirely from an impurity of Co_2B , this value corresponds to $9.5 \times 10^{-4} \mu_{\text{B}}/\text{f.u.}$, or about 0.06% Co_2B impurity given a moment of $1.56 \mu_{\text{B}}/\text{f.u.}$ for Co_2B at 4.2 K.⁵⁰ Although the fraction of ferromagnetic impurity is small, the bulk paramagnetism of the sample gives a comparatively weak signal, so the small contribution from the saturation of Co moments is readily visible. Even though the content of the ferromagnetic impurity is only about 0.06%, as much as 6% of the magnetic response at 70 kOe can be attributed to this phase.

To evaluate the temperature-dependence of intrinsic magnetic susceptibility, $M(T)$ was measured at 35 and 70 kOe, fields of sufficient strength to saturate the ferromagnetic impurity, and a Honda-Owen correction was applied to remove the contribution of this impurity (Figure 6a).^{61–63}

$$\chi_{\text{corr}}(T) = \frac{M_{70 \text{ kOe}}(T) - M_{35 \text{ kOe}}(T)}{70 \text{ kOe} - 35 \text{ kOe}}$$

The inverse of susceptibility obtained via the Honda-Owen method was used for fitting with the modified Curie–Weiss equation: $\chi_{\text{corr}}(T) = \chi_0 + C/(T - \theta)$, where a temperature-independent term χ_0 accounts for Pauli paramagnetism of conduction electrons and the diamagnetic contributions of core electrons and the sample holder. The plot of χ_{corr}^{-1} vs T is nearly linear from 15 to 300 K (inset to Figure 6a). However, the modified Curie–Weiss equation does not give an adequate fit over the entire range owing to slight irregularities in the

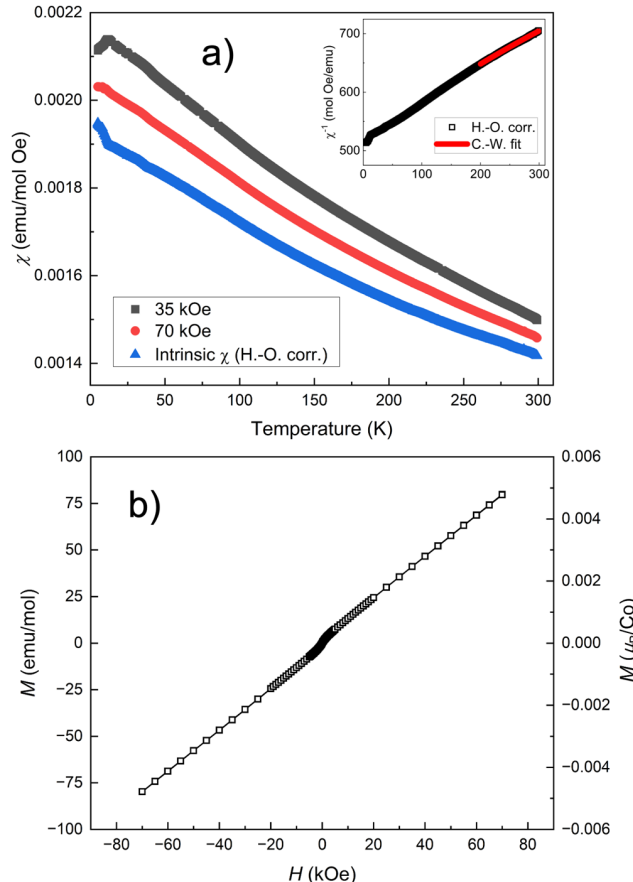


Figure 6. (a) Measured susceptibility $\chi(T)$ at 35 kOe (gray) and 70 kOe (red) fields, and intrinsic susceptibility $\chi_{\text{corr}}(T)$ obtained using the Honda-Owen method to correct for a trace amount of ferromagnetic impurity; inset: fit of inverse susceptibility (χ_{corr}^{-1}) between 200 and 300 K with the modified Curie–Weiss equation yielding fitted parameters $\chi_0 = 6.2(2) \times 10^{-4}$ emu/mol Oe, $C = 0.59(3)$ emu K/mol Oe, and $\theta = -443(16)$ K. (b) Isothermal $M(H)$ at 300 K, with a small saturation at low field indicative of a ferromagnetic impurity.

inflection of the curve. Moreover, the parameters of the Curie–Weiss fit depend strongly on the temperature range used for the fitting, most likely a consequence of a substantial temperature-independent term. In fitting selected data in ranges between 100 and 300 K, a remarkably large magnitude for the Weiss constant θ between -500 and -200 K is obtained with a considerable contribution from the temperature-independent term χ_0 ranging between 5×10^{-4} and 9×10^{-4} emu/mol Oe, while the Curie constant C is found between 0.3 and 0.7 emu K/mol Oe (inset to Figure 6a). The considerable contribution from the temperature-independent term to the total magnitude of susceptibility indicates Pauli paramagnetism, in agreement with the other paramagnetic MCo_3B_2 compounds (vide infra) and the metallic nature of MgCo_3B_2 . The large magnitude of the Weiss constant can point to magnetic frustration or spin-glass behavior but can also indicate that a Curie–Weiss fit is not suitable for the data due to a substantial temperature-independent contribution to the total susceptibility.^{64,65} It should be noted that ZFC/FC splitting of χ at low temperatures, if present, would be difficult to observe since below 39 K the strong diamagnetism of superconducting MgB_2 dominates the measurement. Further-

more, the *ac* susceptibility measured at three different frequencies in a 1000 Oe *dc* bias field in the range 2–50 K (**Figures S18 and S19**) is dominated by the contribution from the MgB₂ impurity since the real component of *ac* susceptibility decreases below the superconducting transition temperature of MgB₂ (**Figure S18**).

It may be insightful to compare the magnetic properties of MgCo₃B₂ with other members of the MCo₃B₂ family. Most of the reported MCo₃B₂ compounds include a rare-earth element in the *M* site. Of those for which magnetic susceptibility has been measured over a range of temperatures, the Gd, Dy, Tb, and Ho compounds exhibit a ferromagnetic transition between 10 and 60 K with Curie–Weiss behavior above the transition;^{66–69} the Sm compound features a potential ferrimagnetic transition at 43 K and Van Vleck paramagnetic behavior above the transition;^{66,70} while the Y and Ce compounds appear to be Pauli (temperature-independent) paramagnets to the lowest measured temperatures.^{66,71,72} In most of these cases, an anomaly is observed at 150–160 K, which is attributed variously to ordering or spin fluctuations of the Co sublattice⁷³ or a ferromagnetic impurity phase. In our analysis, the ubiquity of this feature, the variability in its relative intensity between samples of the same compound, as well as the low saturation moment reported for YCo₃B₂ at 5 K^{66,71} make the impurity explanation the most plausible. The measured intrinsic magnetic susceptibility (after Honda–Owen correction) for MgCo₃B₂ is on the same order of magnitude compared to the reported values for paramagnetic YCo₃B₂ and CeCo₃B₂, as well as susceptibility for SmCo₃B₂, GdCo₃B₂, and DyCo₃B₂ arising only from the Co sublattice, estimated using the deviation from ideal Van Vleck or Curie–Weiss behavior (**Table 3**).⁶⁶ Comparison with ZrCo₃B₂ and HfCo₃B₂ would

Table 3. Room-Temperature (300 K) or Temperature-Independent Contributions to the Magnetic Susceptibility of Various MCo₃B₂ Compounds^a

	susceptibility (measured) (emu/mol Oe)	Co-sublattice susceptibility (calculated) (emu/mol Oe)
MgCo ₃ B ₂	1.42×10^{-3}	
YCo ₃ B ₂	3.5×10^{-3}	
CeCo ₃ B ₂	5.42×10^{-4}	
SmCo ₃ B ₂		3.8×10^{-4}
GdCo ₃ B ₂		7.1×10^{-4}
DyCo ₃ B ₂		1.4×10^{-3}

^aFor MgCo₃B₂ (this work), χ at 300 K (after Honda–Owen correction) is given; for YCo₃B₂, χ at 300 K is estimated from a plot of χ vs. T ,⁷³ while for the remaining compounds, the paramagnetic contributions are converted from reported values that are assumed to be temperature-independent.^{66,72}

likely be insightful since Zr and Hf, like Mg, are not expected to contribute to the magnetic response of the ternary phase. In addition, these are the only other MCo₃B₂ compounds where *M* is not a rare-earth metal, the Co Kagomé network is rumpled, and B–B dimers exist. Unfortunately, magnetic data on these compounds do not seem to be available.

To explore the energetic favorability of magnetic ordering in MgCo₃B₂ in two ordered structure types, band structures were calculated for the CeCo₃B₂ and MgNi₃B₂ structure types using spin-polarized DFT after structural relaxation (**Table 2**). For MgCo₃B₂ in the CeCo₃B₂ and the MgNi₃B₂ structure types, the DFT predicted ground state appears to be nonmagnetic,

i.e., no ordering of local magnetic moments. However, unusual low-lying excited metastable ferromagnetic and antiferromagnetic states were found with only slightly higher formation energies (see **Table 2**). For the ferromagnetic structure, spin-polarized DFT calculations predict a moment of 0.17 μ_B /Co1 atom and 0.41 μ_B /Co2 atom for an average of 0.33 μ_B /Co across the two Co sites. For the antiferromagnetic structure used for calculations, parallel ordering of spins within a single Co Kagomé layer and antiparallel ordering between adjacent layers (collinear spins) was considered. Antiferromagnetic states with noncollinear spins as predicted for some Kagomé compounds with noninteracting layers were not practical to consider using full-potential DFT in VASP. The predicted metastable collinear states should be taken with some caution as DFT does not take into account spin fluctuations (zero-point motion). The energy of these spin fluctuations is typically >10 meV/atom,⁷⁴ which is much larger than the obtained magnetic stabilization energies of our system (<1 meV/atom). In addition, disordered structures (including possible paramagnetic local moment structures) were not considered, and the extent to which conclusions can be drawn regarding the magnetic nature of MgCo₃B₂ is limited. Nevertheless, the nonmagnetic ground state of MgCo₃B₂ at $T = 0$ K from the DFT calculations ultimately supports the experimentally observed non-Curie–Weiss behavior of susceptibility. The evidence presented herein cannot eliminate the possibility of antiferromagnetic order occurring above room temperature or a frustrated/spin glass state. Further investigation into the magnetic nature of this phase, including high-temperature magnetometry, ¹¹B solid-state NMR, magnetic Pair Distribution Function (PDF), heat capacity, and crystal growth could shed light on the intrinsic magnetic nature of this new boride.

CONCLUSIONS

Guided by *in situ* diffraction to probe the mechanism of solid-state reactions and DFT predictions of structure stability, the synthesis of a new intermetallic ternary boride MgCo₃B₂ has been accomplished using a magnesium hydride precursor MgH₂. MgCo₃B₂ is the first ternary compound reported in the Mg–Co–B system, adding another member to MT₃B₂ family of intermetallic borides. Although the hydride route allows the solid-state reaction to proceed more quickly due to the intimate mixing of reactive precursors, synthesis with equivalent yield can be achieved with an elemental Mg precursor; the latter route was used to grow a crystal of MgCo₃B₂ for structural characterization. The structure of MgCo₃B₂ is a disordered variant of the CeCo₃B₂ structure type, featuring a covalent framework that hosts Mg ions in its channels. The disorder associated with Co and B split sites leads to a rumpling of the Co Kagomé network and covalent B–B dimers, structural motifs uncharacteristic of the CeCo₃B₂ prototype. Such bonding motifs of the MgCo₃B₂ phase are very similar to those of chiral intermetallic MgNi₃B₂, but no indications of an ordered superstructure were found in the single-crystal or high-resolution powder diffraction experiments. In-situ X-ray diffraction allowed us to pinpoint an optimal synthesis temperature of 1023 K and showed that the formation of the ternary phase proceeds via an intermediate of Mg₆Co₂H₁₁. Magnetic measurements revealed low magnetization with a weak temperature dependence, consistent with the considerable contribution of the temperature-independent

term of a Curie–Weiss fit and the predicted metallic and nonmagnetic ground state from DFT calculations.

This work highlights the utility of a multifaceted approach to the discovery of new solids in previously empty phase spaces. Crucial to this approach is the use of Rietveld analysis in examining *in situ* PXRD data collected upon heating of precursors mixture to identify peaks corresponding to potentially new compounds, as well as DFT assessment of their stability. *In situ* reaction monitoring provides direction as to the temperature range favorable for synthesis. Optimization of synthesis parameters is enabled by the rapid, diffusion-enhanced hydride route to provide essential experimental validation of a compound's stability via high-yield *ex situ* synthesis, while single crystal XRD in combination with synchrotron PXRD permitted accurate structure determination. Future studies will use this complex approach to screen for other ternary compounds in this and similar systems in search of new borides with distinctive magnetic properties.

■ ASSOCIATED CONTENT

Supporting Information

The Supporting Information is available free of charge at <https://pubs.acs.org/doi/10.1021/acs.chemmater.4c01999>.

Additional tables with parameters of XRD data collection and refinement, tables and plots of PXRD phase analysis, additional structural information and graphics, results of DFT calculations, and additional magnetic measurements ([PDF](#))

MgCo_3B_2 crystallographic information ([CIF](#))

■ AUTHOR INFORMATION

Corresponding Author

Julia V. Zaikina – Department of Chemistry, Iowa State University, Ames, Iowa 50011, United States;  orcid.org/0000-0002-8755-1926; Email: yzaikina@iastate.edu

Authors

Paul Oftedahl – Department of Chemistry, Iowa State University, Ames, Iowa 50011, United States

Nawsher J. Parvez – Department of Physics and Astronomy, University of Delaware, Newark, Delaware 19716, United States

Zhen Zhang – Department of Physics and Astronomy, Iowa State University, Ames, Iowa 50011, United States;  orcid.org/0009-0001-0810-8054

Yang Sun – Department of Physics, Xiamen University, Xiamen 361005, China

Vladimir Antropov – Department of Physics and Astronomy, Iowa State University, Ames, Iowa 50011, United States; U.S. Department of Energy, Ames National Laboratory, Ames, Iowa 50011, United States

John Q. Xiao – Department of Physics and Astronomy, University of Delaware, Newark, Delaware 19716, United States;  orcid.org/0000-0001-7805-8155

Complete contact information is available at:

<https://pubs.acs.org/10.1021/acs.chemmater.4c01999>

Funding

Financial support from the U.S. Department of Energy (DOE) Established Program to Stimulate Competitive Research (EPSCoR) Grant No. DE-SC0024284 is gratefully acknowledged. The Ames Laboratory is operated for the U.S.

Department of Energy by Iowa State University under contract #DE-AC02-07CH11358. This research used resources of the Advanced Photon Source, a U.S. Department of Energy (DOE) Office of Science user facility operated for the DOE Office of Science by Argonne National Laboratory under Contract No. DE-AC02-06CH11357. This research used beamline 28-ID-2 of the National Synchrotron Light Source II, a U.S. Department of Energy (DOE) Office of Science User Facility operated for the DOE Office of Science by Brookhaven National Laboratory under Contract No. DE-SC0012704. Part of the research described in this paper was performed at the Canadian Light Source, a national research facility of the University of Saskatchewan, which is supported by the Canada Foundation for Innovation (CFI), the Natural Sciences and Engineering Research Council (NSERC), the Canadian Institutes of Health Research (CIHR), the Government of Saskatchewan, and the University of Saskatchewan.

Notes

The authors declare no competing financial interest.

■ ACKNOWLEDGMENTS

We thank Dr. Wenqian Xu at beamline 17-BM APS ANL, Dr. Jianming Bai and Dr. Hui Zhong at 28-ID-2 NSLS-II BNL for assisting with the respective *in situ* data collection experiments. We also thank Dr. Adam Leontowich at WLE BXDS CLS for assistance with planning and completing the high-resolution powder X-ray diffraction experiment. We thank Prof. Kirill Kovnir (Chemistry, Iowa State University and Ames National Laboratory) for access to DSC and PXRD instruments and discussions; additionally, we are grateful to Dr. Arkady Ellern (Chemistry, Iowa State University) for assistance in collecting SCXRD data. We also thank Zhijie (Hugh) Chen and Prof. Kai Liu (Department of Physics, Georgetown University) for performing magnetic measurements.

■ REFERENCES

- (1) Akopov, G.; Yeung, M. T.; Kaner, R. B. Rediscovering the Crystal Chemistry of Borides. *Adv. Mater.* **2017**, *29*, No. 1604506.
- (2) Albert, B.; Hillebrecht, H. Boron: Elementary Challenge for Experimenters and Theoreticians. *Angew. Chem., Int. Ed.* **2009**, *2*, 8640–8668.
- (3) Fokwa, B. P. T. Borides: Solid-State Chemistry. In *Encyclopedia of Inorganic and Bioinorganic Chemistry*; Wiley: 2014; pp 1–14.
- (4) Park, H.; Encinas, A.; Scheifers, J. P.; Zhang, Y.; Fokwa, B. P. T. Boron-Dependency of Molybdenum Boride Electrocatalysts for the Hydrogen Evolution Reaction. *Angew. Chem. Int. Ed.* **2017**, *56*, 5575–5578.
- (5) Herbst, J. F.; Croat, J. J.; Pinkerton, F. E.; Yelon, W. B. Relationships between Crystal Structure and Magnetic Properties in $\text{Nd}_2\text{Fe}_{14}\text{B}$. *Phys. Rev. B* **1984**, *29* (7), 4176–4178.
- (6) Lamichhane, T. N.; Xiang, L.; Lin, Q.; Pandey, T.; Parker, D. S.; Kim, T. H.; Zhou, L.; Kramer, M. J.; Bud'Ko, S. L.; Canfield, P. C. Magnetic Properties of Single Crystalline Itinerant Ferromagnet AlFe_2B_2 . *Phys. Rev. Mater.* **2018**, *2* (8), No. 084408.
- (7) Tan, X.; Chai, P.; Thompson, C. M.; Shatruk, M. Magnetocaloric Effect in AlFe_2B_2 : Toward Magnetic Refrigerants from Earth-Abundant Elements. *J. Am. Chem. Soc.* **2013**, *135* (25), 9553–9557.
- (8) Nagamatsu, J.; Nakagawa, N.; Muranaka, T.; Zenitani, Y.; Akimitsu, J. Superconductivity at 39 K in Magnesium Diboride. *Nature* **2001**, *401*, 63–64.
- (9) Gabani, S.; Flachbart, K.; Siemensmeyer, K.; Mori, T. Magnetism and Superconductivity of Rare Earth Borides. *J. Alloys Compd.* **2020**, *821*, No. 153201.

- (10) Mori, T. Thermoelectric and Magnetic Properties of Rare Earth Borides: Boron Cluster and Layered Compounds. *J. Solid State Chem.* **2019**, *275*, 70–82.
- (11) Bhaskar, G.; Gvozdetskyi, V.; Carnahan, S. L.; Wang, R.; Mantravadi, A.; Wu, X.; Ribeiro, R. A.; Huang, W.; Rossini, A. J.; Ho, K. M.; Canfield, P. C.; Lebedev, O. I.; Zaikina, J. V. Path Less Traveled: A Contemporary Twist on Synthesis and Traditional Structure Solution of Metastable LiNi₁₂B₈. *ACS Materials Au* **2022**, *2*, 614.
- (12) Gvozdetskyi, V.; Bhaskar, G.; Batuk, M.; Zhao, X.; Wang, R.; Carnahan, S. L.; Hanrahan, M. P.; Ribeiro, R. A.; Canfield, P. C.; Rossini, A. J.; Wang, C. Z.; Ho, K. M.; Hadermann, J.; Zaikina, J. V. Computationally Driven Discovery of a Family of Layered LiNiB Polymorphs. *Angew. Chem. Int. Ed.* **2019**, *58* (44), 15855–15862.
- (13) Gvozdetskyi, V.; Hanrahan, M. P.; Ribeiro, R. A.; Kim, T. H.; Zhou, L.; Rossini, A. J.; Canfield, P. C.; Zaikina, J. V. A Hydride Route to Ternary Alkali Metal Borides: A Case Study of Lithium Nickel Borides. *Chem. – Eur. J.* **2019**, *25* (16), 4123–4135.
- (14) Stadelmaier, H. H.; Draughn, R. A.; Hofer, G. Die Struktur Der Ternären Boride Vom Chromkarbid-(Cr₂₃C₆)-Typ. *Z. Metallkd.* **1963**, *54* (11), 640–644.
- (15) Adeyemi, A. N.; Bhaskar, G.; Cox, T.; Hong, S.; Gvozdetskyi, V.; Zaikina, J. V. Hydride Precursors in Materials Synthesis. In *Comprehensive Inorganic Chemistry III*, 3rd ed.; Elsevier: 2023; Vol. 1–10, pp 128–146.
- (16) Mantravadi, A.; Gvozdetskyi, V.; Sarkar, A.; Mudryk, Y.; Zaikina, J. V. Exploring the A -V-Sb Landscape beyond AV₃Sb₅: A Case Study on the KV₆Sb₆ Kagome Compound. *Phys. Rev. Mater.* **2023**, *7* (11), No. 115002.
- (17) Gvozdetskyi, V.; Wang, R.; Xia, W.; Zhang, F.; Lin, Z.; Ho, K. M.; Miller, G.; Zaikina, J. V. How to Look for Compounds: Predictive Screening and in Situ Studies in Na–Zn–Bi System. *Chem. – Eur. J.* **2021**, *27* (64), 15954–15966.
- (18) Kovnir, K. Predictive Synthesis. *Chem. Mater.* **2021**, *33*, 4835–4841.
- (19) Bhaskar, G.; Behera, R. K.; Gvozdetskyi, V.; Carnahan, S. L.; Ribeiro, R. A.; Oftedahl, P.; Ward, C.; Canfield, P. C.; Rossini, A. J.; Huang, W.; Zaikina, J. V. Breaking New Ground: MBene Route toward Selective Vinyl Double Bond Hydrogenation in Nitroarenes. *J. Am. Chem. Soc.* **2023**, *145* (50), 27459–27470.
- (20) Bhaskar, G.; Gvozdetskyi, V.; Batuk, M.; Wiaderek, K. M.; Sun, Y.; Wang, R.; Zhang, C.; Carnahan, S. L.; Wu, X.; Ribeiro, R. A.; Bud'ko, S. L.; Canfield, P. C.; Huang, W.; Rossini, A. J.; Wang, C. Z.; Ho, K. M.; Hadermann, J.; Zaikina, J. V. Topochemical Deintercalation of Li from Layered LiNiB: Toward 2D MBene. *J. Am. Chem. Soc.* **2021**, *143* (11), 4213–4223.
- (21) Wang, R.; Sun, Y.; Gvozdetskyi, V.; Zhao, X.; Zhang, F.; Xu, L. H.; Zaikina, J. V.; Lin, Z.; Wang, C. Z.; Ho, K. M. Theoretical Search for Possible Li-Ni-B Crystal Structures Using an Adaptive Genetic Algorithm. *J. Appl. Phys.* **2020**, *127* (9), No. 094902.
- (22) Sun, J.; Wang, R.; Ding, Z.; Zhang, X.; Zhang, Q.; Zhang, B.; Dong, H.; Wu, F. Layered Li-Co-B as a Low-Potential Anode for Lithium-Ion Batteries. *Inorg. Chem.* **2023**, *62* (21), 8136–8144.
- (23) Jung, W. Darstellung Und Kristallstruktur von MgNi₂SB₂ und Li_{1.2}Ni_{2.5}B₂. *Z. Naturforsch.* **1977**, *32b*, 1371–1374.
- (24) Manfrinetti, P.; Pani, M.; Dhar, S. K.; Kulkarni, R. Structure, Transport and Magnetic Properties of MgNi₃B₂. *J. Alloys Compd.* **2007**, *428* (1–2), 94–98.
- (25) Meschke, V.; Gorai, P.; Stevanović, V.; Toberer, E. S. Search and Structural Featurization of Magnetically Frustrated Kagome Lattices. *Chem. Mater.* **2021**, *33* (12), 4373–4381.
- (26) Wilson, S. D.; Ortiz, B. R. AV₃Sb₅ Kagome Superconductors. *Nature Reviews Materials* **2024**, *9*, 420.
- (27) Ye, L.; Kang, M.; Liu, J.; Von Cube, F.; Wicker, C. R.; Suzuki, T.; Jozwiak, C.; Bostwick, A.; Rotenberg, E.; Bell, D. C.; Fu, L.; Comin, R.; Checkelsky, J. G. Massive Dirac Fermions in a Ferromagnetic Kagome Metal. *Nature* **2018**, *555* (7698), 638–642.
- (28) Li, M.; Wang, Q.; Wang, G.; Yuan, Z.; Song, W.; Lou, R.; Liu, Z.; Huang, Y.; Liu, Z.; Lei, H.; Yin, Z.; Wang, S. Dirac Cone, Flat Band and Saddle Point in Kagome Magnet YMn₆Sn₆. *Nat. Commun.* **2021**, *12* (1), 3129.
- (29) Jovanovic, M.; Schoop, L. M. Simple Chemical Rules for Predicting Band Structures of Kagome Materials. *J. Am. Chem. Soc.* **2022**, *144* (24), 10978–10991.
- (30) Toby, B. H.; Von Dreele, R. B. GSAS-II: The Genesis of a Modern Open-Source All Purpose Crystallography Software Package. *J. Appl. Crystallogr.* **2013**, *46* (2), 544–549.
- (31) Krause, L.; Herbst-Irmer, R.; Sheldrick, G. M.; Stalke, D. Comparison of Silver and Molybdenum Microfocus X-Ray Sources for Single-Crystal Structure Determination. *J. Appl. Crystallogr.* **2015**, *48* (1), 3–10.
- (32) Sheldrick, G. M. SHELXT - Integrated Space-Group and Crystal-Structure Determination. *Acta Crystallogr. A* **2015**, *71* (1), 3–8.
- (33) Sheldrick, G. M. Crystal Structure Refinement with SHELXL. *Acta Crystallogr. C Struct. Chem.* **2015**, *71*, 3–8.
- (34) Momma, K.; Izumi, F. VESTA 3 for Three-Dimensional Visualization of Crystal, Volumetric and Morphology Data. *J. Appl. Crystallogr.* **2011**, *44* (6), 1272–1276.
- (35) Chupas, P. J.; Chapman, K. W.; Kurtz, C.; Hanson, J. C.; Lee, P. L.; Grey, C. P. A Versatile Sample-Environment Cell for Non-Ambient X-Ray Scattering Experiments. *J. Appl. Crystallogr.* **2008**, *41* (4), 822–824.
- (36) Gamage, E. H.; Greenfield, J. T.; Unger, C.; Kamali, S.; Clark, J. K.; Harmer, C. P.; Luo, L.; Wang, J.; Shatruk, M.; Kovnir, K. Tuning Fe-Se Tetrahedral Frameworks by a Combination of [Fe(en)₃]²⁺ Cations and Cl-Anions. *Inorg. Chem.* **2020**, *59* (18), 13353–13363.
- (37) Kresse, G.; Furthmüller, J. Efficient Iterative Schemes for *Ab Initio* Total-Energy Calculations Using a Plane-Wave Basis Set. *Phys. Rev. B* **1996**, *54* (16), 11169–11186.
- (38) Perdew, J. P.; Burke, K.; Ernzerhof, M. Generalized Gradient Approximation Made Simple. *Phys. Rev. Lett.* **1996**, *77* (18), 3865–3868.
- (39) Blöchl, P. E. Projector Augmented-Wave Method. *Phys. Rev. B* **1994**, *50* (24), 17953–17979.
- (40) Monkhurst, H. J.; Pack, J. D. Special Points for Brillouin-Zone Integrations. *Phys. Rev. B* **1976**, *13* (12), 5188–5192.
- (41) Černý, R.; Bonhomme, F.; Yvon, K.; Fischer, P.; Zolliker, P.; Cox, D. E.; Hewat, A. Hexamagnesium Dicobalt Undecadeuteride Mg₆Co₂D₁₁: Containing [CoD₄]³⁻ and [CoD₅]⁴⁻ Complex Anions Conforming to the 18-Electron Rule. *J. Alloys Compd.* **1992**, *187*, 233–241.
- (42) Gennari, F. C.; Castro, F. J. Formation, Composition and Stability of Mg-Co Compounds. *J. Alloys Compd.* **2005**, *396* (1–2), 182–192.
- (43) Yoshida, M.; Bonhomme, F.; Yvon, K.; Fischer, P. On the Composition and Structure of the Cubic δ-Phase in the Mg-Co-H System. *J. Alloys Compd.* **1993**, *190* (2), L45–L46.
- (44) Buschow, K. H. J.; Van Engen, P. G.; Jongebreur, R. Magneto-Optical Properties of Metallic Ferromagnetic Materials. *J. Magn. Magn. Mater.* **1983**, *38* (1), 1–22.
- (45) Curtarolo, S.; Setyawan, W.; Hart, G. L. W.; Jahnatek, M.; Chepulskii, R. V.; Taylor, R. H.; Wang, S.; Xue, J.; Yang, K.; Levy, O.; Mehl, M. J.; Stokes, H. T.; Demchenko, D. O.; Morgan, D. AFLOW: An Automatic Framework for High-Throughput Materials Discovery. *Comput. Mater. Sci.* **2012**, *58*, 218–226.
- (46) Jain, A.; Ong, S. P.; Hautier, G.; Chen, W.; Richards, W. D.; Dacek, S.; Cholia, S.; Gunter, D.; Skinner, D.; Ceder, G.; Persson, K. A. Commentary: The Materials Project: A Materials Genome Approach to Accelerating Materials Innovation. *APL Mater.* **2013**, *1*, No. 011002.
- (47) Kirklin, S.; Saal, J. E.; Meredig, B.; Thompson, A.; Doak, J. W.; Aykol, M.; Rühl, S.; Wolverton, C. The Open Quantum Materials Database (OQMD): Assessing the Accuracy of DFT Formation Energies. *NPJ. Comput. Mater.* **2015**, *1*, 15010.
- (48) Saal, J. E.; Kirklin, S.; Aykol, M.; Meredig, B.; Wolverton, C. Materials Design and Discovery with High-Throughput Density

- Functional Theory: The Open Quantum Materials Database (OQMD). *JOM* **2013**, *65* (11), 1501–1509.
- (49) Gates-Rector, S.; Blanton, T. The Powder Diffraction File: A Quality Materials Characterization Database. *Powder Diffr* **2019**, *34* (4), 352–360.
- (50) Villars, P.; Cenzual, K. *Pearson's Crystal Data—Crystal Structure Database for Inorganic Compounds*; ASM International: Materials Park, OH, USA, 2016.
- (51) Zagorac, D.; Muller, H.; Ruehl, S.; Zagorac, J.; Rehme, S. Recent Developments in the Inorganic Crystal Structure Database: Theoretical Crystal Structure Data and Related Features. *J. Appl. Crystallogr.* **2019**, *52*, 918–925.
- (52) Leeman, J.; Liu, Y.; Stiles, J.; Lee, S. B.; Bhatt, P.; Schoop, L. M.; Palgrave, R. G. Challenges in High-Throughput Inorganic Materials Prediction and Autonomous Synthesis. *PRX Energy* **2024**, *3* (1), No. 011002.
- (53) Kuz'ma, Yu. B.; Kripyakevich, P. I.; Bilonizhko, N. S. Crystal Structure of CeCo₃B₂ and Analogous Compounds. *Dopovidi Akademii Nauk Ukrains'koi RSR, Seriya A: Fizyko-Tekhnichni ta Matematichni Nauki* **1969**, *31* (10), 939–941.
- (54) Voroshilov, Yu. V.; Kuz'ma, Yu. B. Reaction of Zirconium with the Transition Metals and Boron. *Soviet. Powder Metallurgy and Metal Ceramics* **1969**, *8* (11), 941–944.
- (55) Alekseeva, A. M.; Abakumov, A. M.; Chizhov, P. S.; Leithe-Jasper, A.; Schnelle, W.; Prots, Y.; Hadermann, J.; Antipov, E. V.; Grin, Y. Ternary Magnesium Rhodium Boride Mg₂Rh_{1-x}B_{6+2x} with a Modified Y₂ReB₆-Type Crystal Structure. *Inorg. Chem.* **2007**, *46* (18), 7378–7386.
- (56) Rogl, P. Über SE-Metall - Kobaltboride. *Monatsh. Chem.* **1973**, *104* (6), 1623–1631.
- (57) Stokes, H. T.; Hatch, D. M. FINDSYM: Program for Identifying the Space-Group Symmetry of a Crystal. *J. Appl. Crystallogr.* **2005**, *38*, 237–238.
- (58) Stokes, H. T.; Hatch, D. M.; Campbell, B. J. FINDSYM, ISOTROPY Software Suite. iso.byu.edu.
- (59) Wu, S. Q.; Ji, M.; Wang, C. Z.; Nguyen, M. C.; Zhao, X.; Umemoto, K.; Wentzcovitch, R. M.; Ho, K. M. An Adaptive Genetic Algorithm for Crystal Structure Prediction. *J. Phys.: Condens. Matter* **2014**, *26* (3), No. 035402.
- (60) Kanomata, T.; Ise, Y.; Kumagai, N.; Haga, A.; Kamishima, K.; Goto, T.; Kimura, H. M.; Yoshida, H.; Kaneko, T.; Inoue, A. Magnetovolume Effect of Co₂B. *J. Alloys Compd.* **1997**, *259* (1–2), L1–L4.
- (61) Owen, M. Magnetochemische Untersuchungen. Die Thermo-magnetischen Eigenschaften Der Elemente. *Ann. Phys.* **1912**, *342*, 657–699.
- (62) Honda, K. Die Thermomagnetischen Eigenschaften Der Elemente. *Ann. Phys.* **1910**, *337*, 1027–1063.
- (63) Yang, J.; Matsui, M.; Kawa, M.; Ohta, H.; Michioka, C.; Dong, C.; Wang, H.; Yuan, H.; Fang, M.; Yoshimura, K. Magnetic and Superconducting Properties in Single Crystalline Fe_{1+δ}Te_{1-x}Se_x ($x < 0.50$) System. *J. Phys. Soc. Jpn.* **2010**, *79* (7), No. 074704.
- (64) Mydosh, J. A. *Spin Glasses*, 1st ed., eBook; CRC Press: London, 2014.
- (65) Siebeneichler, S.; Ovchinnikov, A.; Sheptyakov, D.; Mudring, A. V. Making a Hedgehog Spin-Vortex State Possible: Geometric Frustration on a Square Lattice. *Chem. Mater.* **2024**, *36* (8), 3546–3554.
- (66) Ido, H.; Nanjo, M.; Yamada, M. Magnetic Susceptibility of RC_o₃B₂ (R = Y, Sm, Gd, and Dy). *J. Appl. Phys.* **1994**, *75* (10), 7140–7142.
- (67) Caspi, E. N.; Dubman, M.; Ettedgui, H.; Shaked, H.; Short, S.; Jorgensen, J. D. Magnetic and Crystallographic Properties of HoCo₃B₂. *In Physica B: Condensed Matter* **2005**, *359–361*, 944–946.
- (68) Zheng, X. Q.; Xu, J. W.; Zhang, H.; Zhang, J. Y.; Wang, S. G.; Zhang, Y.; Xu, Z. Y.; Wang, L. C.; Shen, B. G. Magnetic Properties and Magnetocaloric Effect of HoCo₃B₂ Compound. *AIP Adv.* **2018**, *8* (5), No. 056432.
- (69) Li, L.; Huo, D.; Igawa, H.; Nishimura, K. Large Magnetocaloric Effect in TbCo₃B₂ Compound. *J. Alloys Compd.* **2011**, *509* (5), 1796–1799.
- (70) Ido, H.; Yamada, M.; Nashima, O.; Ito, T.; Yoshida, H. Anomalous Magnetic Properties of the Compound SmCo₃B₂. *J. Appl. Phys.* **2000**, *87* (9), 4912–4914.
- (71) Ching, W. Y.; Ido, H.; Yamauchi, H.; Cheng, S. F.; Sankar, S. G.; Wallace, W. E. Magnetism in Elements, Alloys, and Compounds Magnetic Properties of the Y_{1-x}Gd_xCo₃B₂ System. *J. Appl. Phys.* **1991**, *70* (10), 6540–6542.
- (72) Yang, K. N.; Torikachvili, M. S.; Maple, M. B.; Ku, H. C. Magnetic Susceptibility of CeT₃B₂ and UT₃B₂ Compounds (T = Co, Ru, and Ir). *J. Appl. Phys.* **1985**, *57* (8), 3140–3142.
- (73) Ballou, R.; Burzo, E.; Pop, V. Magnetic Properties of (Gd_xY_{1-x})Co₃B₂ Compounds. *J. Magn Magn Mater.* **1995**, *140–144*, 945–946.
- (74) Wysocki, A. L.; Valmispild, V. N.; Kutepov, A.; Sharma, S.; Dewhurst, J. K.; Gross, E. K. U.; Lichtenstein, A. I.; Antropov, V. P. Spin-Density Fluctuations and the Fluctuation-Dissipation Theorem in 3d Ferromagnetic Metals. *Phys. Rev. B* **2017**, *96* (18), No. 184418.